**Proceedings of the 2003 IEEE International Frequency Control Symposium and PDA Exhibition**
**Jointly with the 17th European Frequency and Time Forum**

# Higher-Mode Free-Free Beam Micromechanical Resonators

Mustafa U. Demirci and Clark T.-C. Nguyen
Center for Integrated Wireless Microsystems (WIMS)
Department of Electrical Engineering and Computer Science
University of Michigan, Ann Arbor, Michigan 48109-2122 USA
TEL: (734)764-3352, FAX: (734)763-9324, email: mdemirci@eecs.umich.edu

***Abstract* - Polysilicon free-free beam micromechanical resonators based on MEMS technology operating in second and third-mode flexural vibrations have been demonstrated at frequencies as high as 102 MHz with *Q*'s on the order of 11,500. Via strategic placement of electrodes, and careful determination of the exact support beam attachment locations that minimize anchor loss, these new resonators actually exhibit higher *Q* in the second mode than in the fundamental at the same frequency. Experiments to gauge the effect of variations in support beam dimensions and attachment locations on free-free beam microresonator performance show that an offset of only 0.6 μm in the support beam attachment location results in a 7X degradation in the *Q*. In addition, measured temperature coefficients for second-mode free-free beam μresonators are on the order of –13.1 ppm/°C, which is on par with that for fundamental mode resonance.**

***Keywords* - anchor loss, free-free beam, higher-mode, micromechanical resonator, motional resistance, quality factor, RF MEMS**

## I. Introduction

Vibrating micromechanical resonators are emerging as attractive candidates for on-chip versions of the high-*Q* mechanical passive components (e.g, quartz crystals, SAW resonators) used in transceivers for wireless communications [1]. Acute interest in these devices arises from their tiny sizes, their zero DC power consumption, and their use of IC-compatible fabrication technologies to enable on-chip integration of high-*Q* frequency selective components with transistor electronics [2]-[4]. To date, flexural-mode free-free beam micromechanical resonators with frequencies up to 92 MHz and *Q*'s exceeding 7,000 have been demonstrated with performance suitable for IF filter applications [5]. However the need for further size reduction to attain even higher frequencies can conjure up scaling-induced problems [6], such as higher motional impedance and greater susceptibility to contaminants. To avoid these limitations, a method for raising frequency without the need for excessive scaling is desired.

Pursuant to reducing the amount of size reduction needed for increasing frequency, this work investigates higher-mode operation of vertical free-free beam micromechanical resonators. With larger dimensions than previous fundamental-mode counterparts at the same frequency, and with slightly higher *Q*'s (as will be seen), these higher-mode free-free beam resonators provide several key advantages over the former, including (1) lower series motional resistance $R_x$; (2) higher dynamic range and power handling; and (3) multiple ports that permit the 0° input-to-output phase-shift often preferred for high impedance micromechanical oscillators and invertible bandpass mixer-filters targeted for wireless applications. This paper first develops a complete model for design and simulation of higher-mode free-free beam micromechanical resonators in Sections II and III,

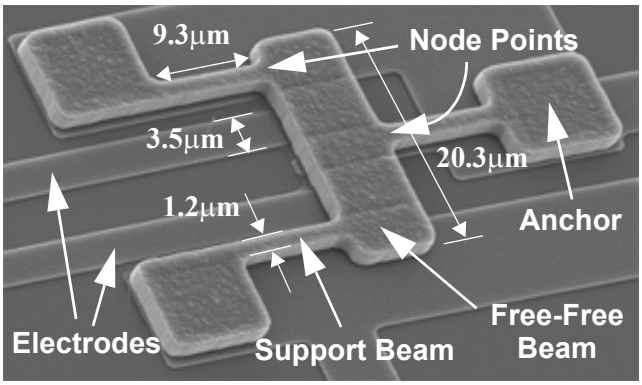


Fig. 1: SEM of a 101 MHz second-mode free-free beam μresonator.

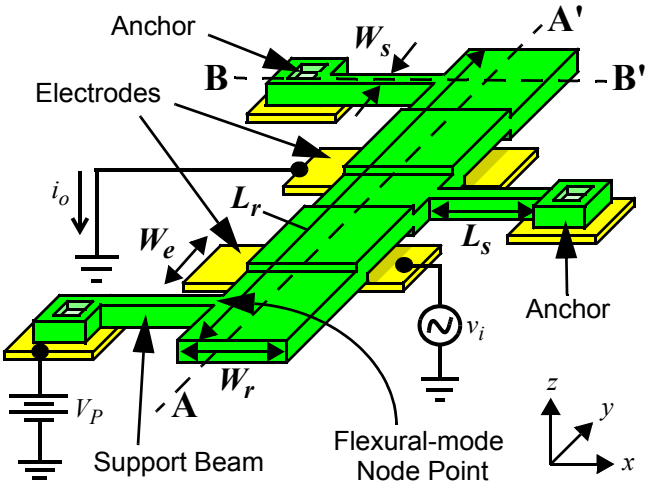


Fig. 2: Perspective-view schematic of a second-mode free-free beam μresonator in a typical bias and excitation configuration.

then verifies the model experimentally in Section IV. In addition to plots verifying performance, Section IV also includes measurements to gauge the effects of dimensional fabrication tolerances on the performance of this precise design, as well as frequency versus temperature data to evaluate thermal stability of this device.

## II. Resonator Structure And Operation

Figure 1 presents the scanning electron micrograph (SEM) of the 101 MHz, second-mode, free-free beam device of this work. Figure 2 presents the perspective view schematic of the device in a typical electrical bias and excitation configuration. As seen in the figure, the device is comprised of a 2 μm thick, free-free beam suspended 1000 Å above capacitive transducer elec-

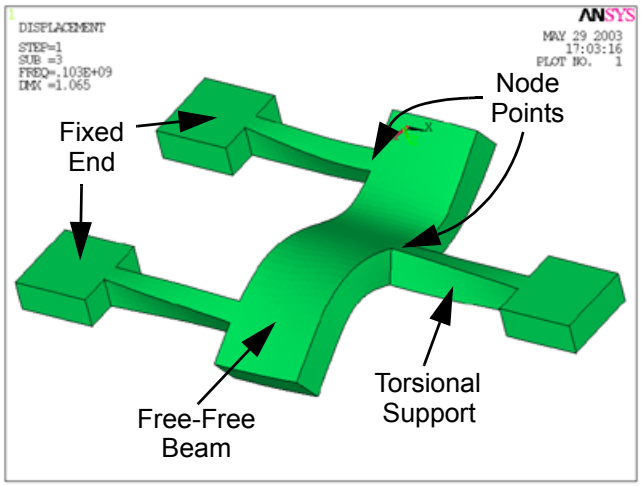


Fig. 3: The flexural vibration mode shape of a second-mode free-free beam μresonator as simulated via ANSYS.

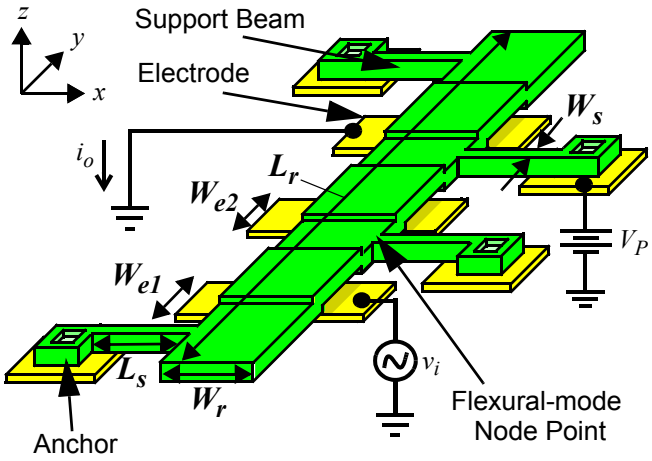


Fig. 4: Perspective-view schematic of a third-mode free-free beam μresonator.in a preferred bias and excitation configuration.

trodes by three support beams designed with dimensions corresponding to a torsional quarter wavelength of the resonator center frequency and attached at precise nodal locations. Two separate electrodes are placed under the device at locations specifically chosen to excite its second flexural vibration mode, shown in Fig. 3. To operate this device, a DC bias $V_P$ is applied to the beam and an AC drive voltage $v_i$ is applied to one of the electrodes. These voltages then collectively create a time-varying electrostatic excitation force between the electrode and the beam, in the vertical direction, and at the frequency of the AC drive voltage if $V_P > v_i$. When the AC drive frequency matches the beam resonance frequency, the force causes the beam to vibrate, which then results in a DC biased time-varying capacitance at the output electrode, which in turn produces an output current $i_o$. It is also possible to excite the fundamental vibration mode of this device using the same electrical configuration, but applying an AC drive voltage at the frequency of the fundamental mode.

Figure 4 presents the perspective view schematic of a third-mode free-free beam μresonator, also realized in this work. This device is similar to the second mode one except it is larger in beam length for the same frequency and is supported by four tor-

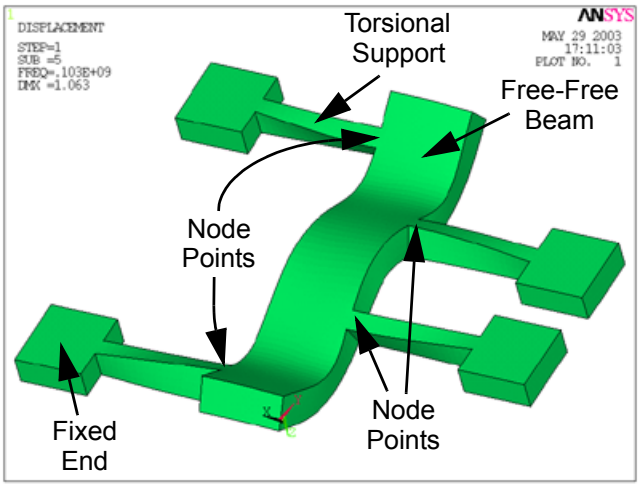


Fig. 5: The flexural vibration mode shape of a third-mode free-free beam μresonator as simulated via ANSYS.

sional-mode quarter wavelength support beams at points intersecting its four nodal lines. The ANSYS simulated mode shape of the device is shown in Fig. 5. The device has three electrodes underneath that can be phased accordingly in order to preferentially excite the third vibration mode.

## III. Higher-Mode Free-Free Beam Resonator Design

The procedure for designing the higher-mode devices of this work involves: (1) selection of resonator beam dimensions for a desired center frequency; (2) determination of the support beam dimensions and free-free beam attachment locations that minimize anchor loss-induced $Q$ degradation; and (3) proper electrode placement to excite higher modes and to achieve the desired input-to-output phase difference. Each step of this procedure is now discussed below.

### *A. Resonator Beam Design*

As with all micromechanical resonators, the center frequency of this free-free beam device is determined by its structural material properties and by its dimensions: width $W_r$, thickness $h$, and the length $L_r$, all of which are indicated in Fig. 2. For practical designs, the beam thickness $h$ is set by fabrication process limitations, and $W_r$ has only a second-order influence on frequency, leaving beam length $L_r$ as the key design parameter to set the resonance frequency. For the case of large $L_r$-to-$W_r$ and $L_r$-to-$h$ ratios, the frequency of the $n^{th}$ vibration mode of a free-free beam can be determined using the Euler-Bernoulli equation, given by [7]

$$f_{nom} = \frac{1}{2\pi\sqrt{12}}(\beta_n L_r)^2 \sqrt{\frac{E}{\rho}}\frac{h}{L_r^2} \qquad (1)$$

where E and ρ are the Young's modulus and density of the structural material, respectively, $h$ and $L_r$ are as indicated in Fig. 2, and $\beta_n$ is the mode coefficient given by the $n^{th}$ root of the equation [7]

$$\cos(\beta_n L_r)\cosh(\beta_n L_r) = 1\,. \qquad (2)$$

For the first three modes $\beta_1 L_r$, $\beta_2 L_r$ and $\beta_3 L_r$ are 4.73, 7.853, and 10.996, respectively.

Again, the above closed-form Euler-Bernoulli equation is accurate only for lower frequency resonators with large $L_r$-to-$W_r$

and $L_r$-to-$h$ ratios. For upper VHF frequency designs, for which $L_r$ begins to approach $h$, Euler-Bernoulli theory loses its accuracy, since it ignores the effects of shearing displacements and rotary inertia. When these effects are important, more complex frequency equations based on Timoshenko theory provide much better accuracy [5]. Thus, the dimensions required to achieve a resonance frequency $f_{nom}$ for a free-free beam with uniform cross-section operating in a symmetric mode (i.e., odd numbered mode, such as the fundamental or the third mode) are best obtained by solving the Timoshenko-derived equation [9]

$$\tan\frac{\beta}{2} + \frac{\beta}{\alpha}\left(\frac{\alpha^2+g^2}{\beta^2-g^2}\right)\tanh\frac{\alpha}{2} = 0 \qquad (3)$$

where

$$g^2 = (2\pi f_o)^2 L_r^2 \frac{\rho}{E}, \qquad (4)$$

$$\left.\begin{matrix}\alpha^2\\ \beta^2\end{matrix}\right\} = \frac{g^2}{2}\left[\mp\left(1+\frac{E}{\kappa G}\right) + \sqrt{\left(1+\frac{E}{\kappa G}\right)^2 + \frac{4L_r^2 h W_r}{g^2 I_r}}\right], \qquad (5)$$

$$G = \frac{E}{2(1+\nu)} \text{ and } I_r = \frac{W_r h^3}{12} \qquad (6)$$

where $G$ and $\nu$ are the shear modulus of elasticity and Poisson's ratio, respectively, of the structural material, $I_r$ is the bending moment of inertia, and $\kappa$ is the shear-deflection coefficient. For a rectangular cross-section, $\kappa$ is 2/3. For antimetric modes (i.e., even numbered mode, such as the second or the fourth mode) the frequency equation is [9]

$$\tan\frac{\beta}{2} - \frac{\alpha}{\beta}\left(\frac{\beta^2-g^2}{\alpha^2+g^2}\right)\tanh\frac{\alpha}{2} = 0 \qquad (7)$$

The variable $f_{nom}$ represents the mechanical resonance frequency for the case of zero DC bias (i.e., $V_P$=0) applied to the resonator body. As described in the past literature [10], the resonance frequency of a capacitively-transduced beam is a function of the DC-bias voltage $V_P$ applied to the resonator body, which effectively introduces an electrical spring stiffness that subtracts from the mechanical stiffness of the beam. The resonance frequency $f_o$ of a free-free beam device including the effect of DC-bias-derived electrical stiffness is given by

$$f_o = f_{nom}\left[1 - \left\langle\frac{k_e}{k_m}\right\rangle\right]^{1/2} \qquad (8)$$

where $\langle k_e/k_m\rangle$ is a parameter representing the effective electrical-to-mechanical stiffness ratio integrated over the electrodes, given by

$$\left\langle\frac{k_e}{k_m}\right\rangle = \sum_{i=1}^{N_e}\int_{L_{i1}}^{L_{i2}} \frac{V_P^2 \varepsilon_o W_r}{d_o^3 k_m(y)}(dy) \qquad (9)$$

where $\varepsilon_o$ is the permittivity in vacuum; $d_o$ is the electrode-to-resonator gap spacing; $k_m(y)$ is the mechanical stiffness as a function of location $y$ on the μresonator beam [8], given by

$$k_m(y) = [2\pi f_{nom}]^2 m_r(y) \qquad (10)$$

where $m_r(y)$ is the equivalent mass at a location $y$, to be given later; $L_{i1}$ and $L_{i2}$ are the start and end locations, respectively, of the $i^{th}$ electrode of the device as illustrated in Fig. 6 for a second-mode resonator (i.e, $n$=2); $N_e$ is the total number of electrodes; where the dependence of electrode-to-resonator gap spacing on $y$ (due to the DC-bias force) has been neglected [8]; and where it has been assumed that all electrodes, whether or not they hold AC signals, are at DC ground.

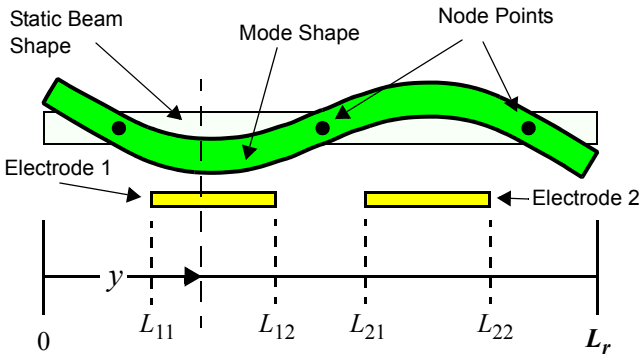


Fig. 6: Cross-section of a second-mode free-free beam resonator, illustrating electrode placement, mode-shape, and node locations.

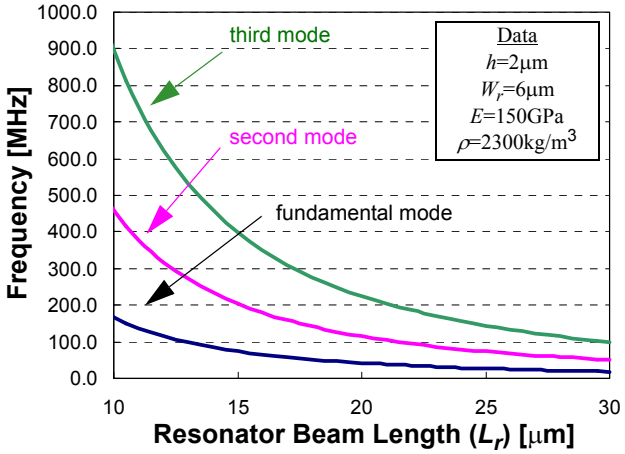


Fig. 7: Simulated plots of frequency versus beam length for free-free beams operating in the fundamental, second, and third modes.

The $n^{th}$ vibration mode shape of a free-free beam resonator can be described by [7]

$$Z_{mode}(y) = \cosh\beta_n y + \cos\beta_n y - \xi[\sinh\beta_n y + \sin\beta_n y] \qquad (11)$$

where

$$\xi = \frac{\cosh\beta_n L_r - \cos\beta_n L_r}{\sinh\beta_n L_r - \sin\beta_n L_r} \qquad (12)$$

and where $Z_{mode}(y)$ is the $z$-directed displacement at location $y$. (See Fig. 2 for axis definitions.)

Figure 7 presents simulated plots, using the above formulations, of frequency versus beam length for free-free beam resonators operating in the fundamental, second, and third modes. As shown, at 100 MHz, operation in the third-mode allows the use of a 2.33X larger beam length than would be required for a beam operating in the fundamental-mode, underscoring the advantages of higher-mode operation.

*B. Support Structure Design*

In order to maximize the $Q$ of a given resonator design, the couplings of resonator vibrations through its supports to its

anchors, and finally, to substrate, must be minimized. To alleviate anchor losses due to translational motion of the resonator beam, the higher-mode free-free beams of this work are supported by torsional-mode beams attached at node points of the mode shape, where ideally no translational motion occurs. These node locations, shown in Fig. 6 for a second-mode free-free beam resonator, are specified via evaluation of (11).

Although the attachment of support beams at nodal locations greatly reduces anchor losses due to translational motion of the resonator beam itself, attachment alone cannot eliminate further losses emanating from torsional motion of the support beams. Losses from torsional motion are strategically prevented by using support beam lengths corresponding to a quarter wavelength of the operating frequency [5]. In principle, the use of quarter-wavelength support dimensions effectively transforms the infinite acoustic impedance seen at the anchors to zero impedance at the resonator attachment locations. In effect, the resonator beam effectively "sees" no supports, and operates as if virtually levitated, with ideally no losses through its supports. The quarter-wavelength condition is met by choosing the dimensions of the torsional support beam to satisfy [12][13]

$$L_s = \frac{1}{4f_o}\sqrt{\frac{G\gamma}{\rho J_s}} \tag{13}$$

where $J_s$ is the polar moment of inertia, given by

$$J_s = \frac{(h^2 + W_s^2)}{12} \tag{14}$$

and $\gamma$ is the torsion constant. For a rectangular cross-section with $h/W_s = 1.75$, $\gamma$ is given by [13]

$$\gamma = 0.214 h W_s^3 . \tag{15}$$

In practice, the utility of the above anchor-isolating design strategies is subject to the finite precision to which support beams can be located and dimensioned. Section IV will present measurements to quantify the degree to which finite process tolerances compromise the effectiveness of the above strategies.

*C. Electrode Design and Equivalent Circuit*

In order to excite the correct mode of a higher-mode free-free beam device, electrodes are situated underneath the resonator and centered between each adjacent node pair, as illustrated for a vibrating second-mode device in Fig. 6. During second mode resonance, shown in Fig. 8(a), the two underlying electrodes couple electrostatically to resonator beam locations that move in opposite directions, allowing the input and output signals of the device to be in phase at resonance (i.e., the output current $i_o$ is equal to the input current $i_i$), thereby allowing the use of the simple *LCR* equivalent circuit model shown in Fig. 8(b). When the device is operated in its fundamental mode as in Fig. 9(a), the portions of the resonator located above the two electrodes move in the same direction causing input and output signals to be out-of-phase (i.e., the output current $i_o$ as defined is equal to the inverse of input current $-i_i$) at resonance. To model this condition an inversely coupled transformer is added to the *LCR* circuit, as shown in Fig. 9(b).

The values of the circuit elements can be determined by appropriate impedance analyses. For the case of identical, purely symmetrical electrodes, each centered between nodal points of the free-free beam, such an analysis yields [8]

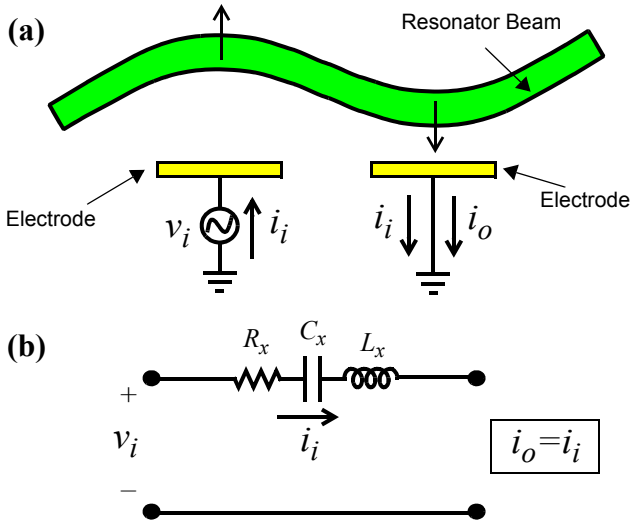


Fig. 8: **(a)** Cross-sectional view of a free-free beam μresonator vibrating in its second mode, indicating the directions of motion above electrodes; and **(b)** its *LCR* equivalent circuit.

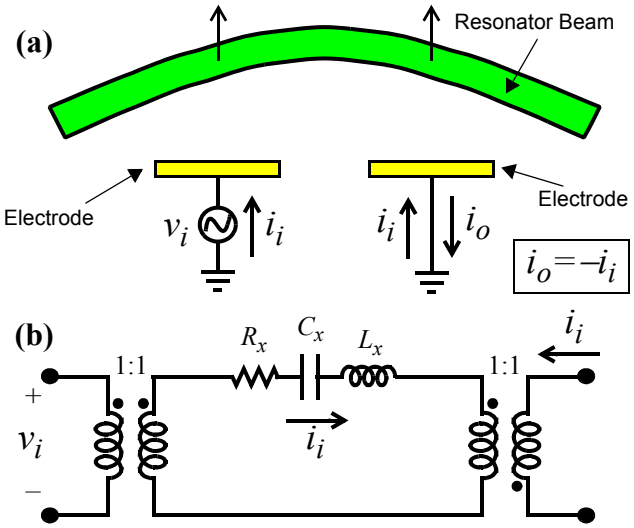


Fig. 9: **(a)** Cross-sectional view of a free-free beam μresonator vibrating in its fundamental mode, indicating the direction of motion above electrodes; and **(b)** its *LCR* equivalent circuit.

$$R_x = \frac{\sqrt{k_{re} m_{re}}}{Q\eta_e^2} \;,\; L_x = \frac{m_{re}}{\eta_e^2} \;,\; C_x = \frac{\eta_e^2}{k_{re}} \tag{16}$$

where $k_{re}$ and $m_{re}$ are the equivalent stiffness and mass at the centers of the electrodes obtained by evaluating [8]

$$m_r(y) = \frac{\rho W_r h \int_0^{L_r} [Z_{mode}(y')]^2 (dy')}{[Z_{mode}(y)]^2} \;,\; k_r(y) = \omega_o^2 m_r(y) \tag{17}$$

at $y$'s corresponding the centers of the electrodes; and $\eta_e$ is the electromechanical coupling factor, given by

$$\eta_e = \sqrt{\int_{L_{OUT}} \int_{L_{IN}} \frac{V_P^2 (\varepsilon_o W_r)^2}{d_o^4} \frac{k_{re}}{k_r(y')} \frac{Z_{mode}(y)}{Z_{mode}(y')} dy' dy} \tag{18}$$

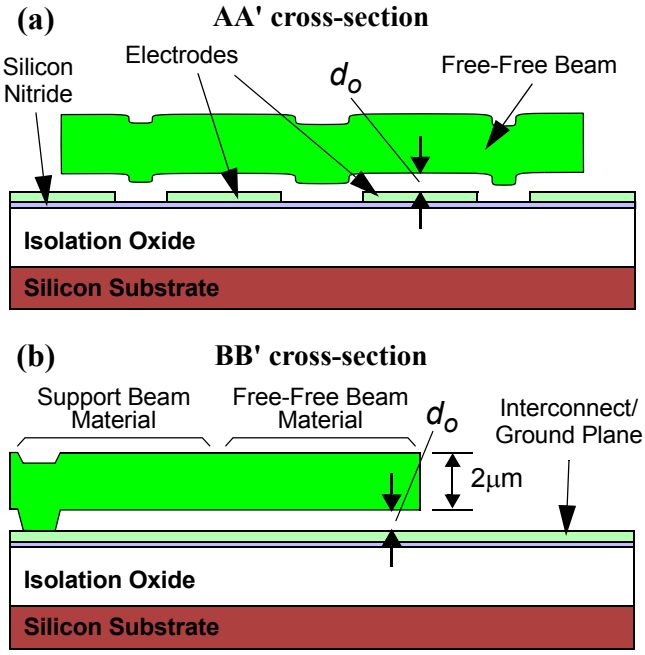


Fig. 10:Final cross-sections for a second-mode free-free beam μresonator along the **(a)** AA' and **(b)** BB' lines defined in Fig. 2.

where $L_{IN}$ and $L_{OUT}$ are the regions specifying the start and end coordinates of the input and output electrodes along the $y$-axis (similar to Fig. 6), respectively; and where the dependence of the electrode-to-resonator gap spacing on $y$ (due to the DC-bias force) has been neglected [8].

The third-mode free-free beam resonator has an advantage over the second mode in greater phase flexibility. In particular, since it has three electrodes, a third-mode resonator can achieve $0^o$ and $180^o$ phase shifted outputs simultaneously. For example, when either one of the side electrodes is chosen as the input electrode, the output current at the middle electrode will have $0^o$ phase while the output current at the other side electrode will have $180^o$ phase relative to the input voltage. The second-mode free-free beam has only two electrodes, so its input-to-output phase difference is fixed at $0^o$, unless the input electrode is split (which would be detrimental, since it would decrease the electrode overlap area, hence, increase $R_x$).

## IV. Experimental Results

Fundamental, second-, and third-mode free-free beam μmechanical resonators with resonance frequencies ranging from 60 MHz to 100 MHz were designed and fabricated in $POCl_3$ doped polysilicon using a small-gap surface-micromachining process similar to those used for previous fundamental-mode free-free beams [5], except that dimples were not used in this process. Final cross sections for a second-mode free-free beam μresonator along two different lines indicated in Fig. 2 are shown in Fig. 10 Figures 11 and 1 present SEM's of fabricated 101 MHz third-mode and a 102 MHz second-mode free-free beam μresonators, respectively. Table I summarizes design and layout data (as well as measured data to be discussed) for fundamental, second-mode, and third-mode free-free beam resonators for comparison purposes.

Since resonator design and performance comparisons will be made shortly, it should be noted that the resonators of Table I are not all from the same wafer. In particular, the 80 MHz resonators came from one wafer, while the 100 MHz resonators came from another. These two wafers were fabricated alongside in the same run, so their sacrificial-oxide layer and structural polysilicon film depositions were done simultaneously in the same LPCVD tube. However, they were released using different etchant procedures, which might explain how they ended up with different extracted [8] electrode-to-resonator gap spacings.

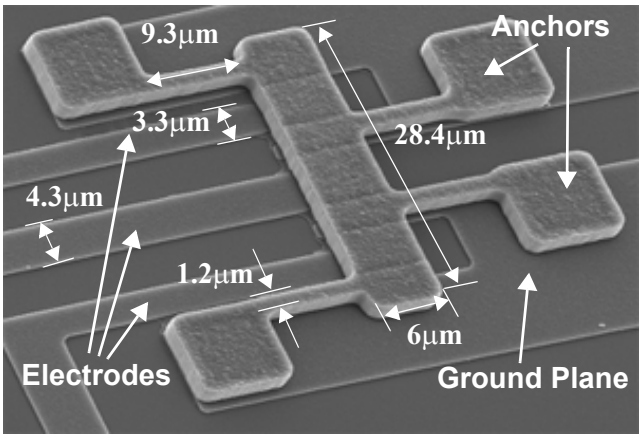


Fig. 11:SEM of a fabricated 102 MHz third-mode free-free beam μresonator.

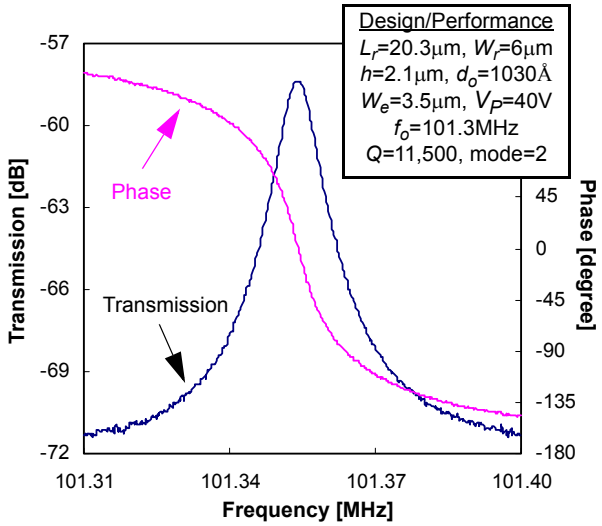


Fig. 12:Frequency response spectrum of a 101 MHz second-mode free-free beam μresonator.

For measurement and characterization, each resonator die was mounted on a printed circuit board and placed in a custom-built vacuum chamber. Electrical access to the circuit board was established via DC and coaxial feedthroughs through a metal block that served as one of the vacuum chamber walls. A turbomolecular vacuum pump provided operating pressures down to 50μTorr, where viscous gas damping [14] is greatly suppressed, allowing resonators under test to exhibit their maximum $Q$'s. Devices were measured using an HP8751A Network Analyzer and S-parameter test set.

Figure 12 presents the second mode frequency characteristics for the device of Fig. 1, measured using the excitation configuration of Fig. 2. The $Q$ of the device is 11,500 at 101.3 MHz, and

**Table I: Higher-mode Free-free Beam Design And Performance Summary**

| | Row No. | Parameter | Source | Vibration Mode | | | | Unit |
|---|---|---|---|---|---|---|---|---|
| | | | | **Fundamental** | **Second** | **Second** | **Third** | |
| Designed/Fabricated/Given | 1 | Target Frequency | design | 80 | 80 | 100 | 100 | MHz |
| | 2 | Resonator Beam Length, $L_r$ | layout | 14.3 | 23.7 | 20.3 | 28.4 | μm |
| | 3 | Resonator Beam Width, $W_r$ | layout | 6 | 6 | 6 | 6 | μm |
| | 4 | Support Beam Length, $L_s$ | layout | 12.3 | 12.3 | 9.3 | 9.3 | μm |
| | 5 | Support Beam Width, $W_s$ | layout | 1.2 | 1.2 | 1.2 | 1.2 | μm |
| | 6 | Node Location 1, $L_{n1}$ | layout | 3.3 | 3.2 | 2.7 | 2.7 | μm |
| | 7 | Node Location 2, $L_{n2}$ | layout | 11.0 | 11.9 | 10.1 | 10.0 | μm |
| | 8 | Node Location 3, $L_{n3}$ | layout | — | 20.5 | 17.6 | 18.3 | μm |
| | 9 | Node Location 4, $L_{n4}$ | layout | — | — | — | 25.7 | μm |
| | 10 | Polysilicon Film Thickness, $h$ | measured | 2.1 | 2.1 | 2.1 | 2.1 | μm |
| | 11 | Effective Resonator Thickness, $h_{eff}$ | adjusted | 2.06 | 2.06 | 1.98 | 2.01 | μm |
| | 12 | Electrode Width, $W_e$ | layout | 3.7 | 4.6 | 3.5 | — | μm |
| | 13 | Side Electrode Width, $W_{e1}$ | layout | — | — | — | 3.3 | μm |
| | 14 | Middle Electrode Width, $W_{e2}$ | layout | — | — | — | 4.3 | μm |
| | 15 | Physical Resonator-to-Electrode Gap, $d_o$ | measured | 1030 | 1030 | 1030 | 1030 | Å |
| | 16 | Young's Modulus, $E$ | measured | 150 | 150 | 150 | 150 | GPa |
| | 17 | Poisson Ratio, $\nu$ | [11] | 0.226 | 0.226 | 0.226 | 0.226 | — |
| Measured | 18 | Measured Frequency, $f_o$ | measured | 79.0 | 78.5 | 101.3 | 102.1 | MHz |
| | 19 | Measured Quality Factor, $Q$ | measured | 13,240 | 15,050 | 11,500 | 4,590 | — |
| | 20 | $V_P$ used in measurement, $V_{Pm}$ | measured | 16 | 16 | 40 | 40 | V |
| | 21 | Measured Series Resistance, $R_x$ | measured | 45 | 27 | 42 | 92 | kΩ |
| Analytical | 22 | Timoshenko Frequency, $f_o$ ($V_P$=$V_{Pm}$) | Eq. (3)-(8) | 79.25 | 78.49 | 101.24 | 102.15 | MHz |
| | 23 | Timoshenko Frequency, $f_o$ ($V_P$=0V) | Eq. (3)-(8) | 79.31 | 78.54 | 101.33 | 102.25 | MHz |
| | 24 | Euler-Bernoulli Frequency, $f_o$ ($V_P$=$V_{Pm}$) | Eq. (1) | 83.56 | 83.86 | 109.84 | 111.69 | MHz |
| | 25 | Euler-Bernoulli Frequency, $f_o$ ($V_P$=0V) | Eq. (1) | 83.62 | 83.92 | 109.94 | 111.80 | MHz |
| | 26 | Calculated Series Resistance, $R_x$ | Eq. (16)-(18) | 39.7 | 32.6 | 42.2 | 92.5 | kΩ |
| | 27 | Adjusted/Extrapolated Gap, $d_o$ | Eq. (8)-(10) | 750 | 750 | 1030 | 925 | Å |

as expected, its input-to-output phase difference at resonance is 0°. The device has also been measured operating in its fundamental mode yielding a $Q$ of 9,850 at 39.2 MHz as shown in Fig. 13. As predicted in Section III and verified in Fig. 13, when operating in its fundamental mode this device has a 180° input-to-output phase difference, caused by placement of the input and output electrodes under portions of the beam that move in phase during resonance. (To obtain an accurate phase response, the phase due to board parasitics was first measured with the resonator's input shorted to its output, then subtracted from the phase response measured with the device present.)

Figure 14 presents the measured frequency response of the third-mode resonator of Fig. 11, showing a $Q$ of 4,980, and having an input-to-output phase difference at resonance of 180°. The inverting phase shift is obtained by driving the resonator at one of its end electrodes, and sensing at the other end electrode, which is positioned under a portion of the resonator beam that moves in phase with that over the drive electrode, as seen in the excitation configuration of Fig. 4. This drive configuration also has the advantage of being able to excite all three modes of this third-mode-designed device. In its first and second modes, this device yields $Q$'s of 10,000 at 22 MHz (first mode) and 9,790 at 53 MHz (second mode), respectively.

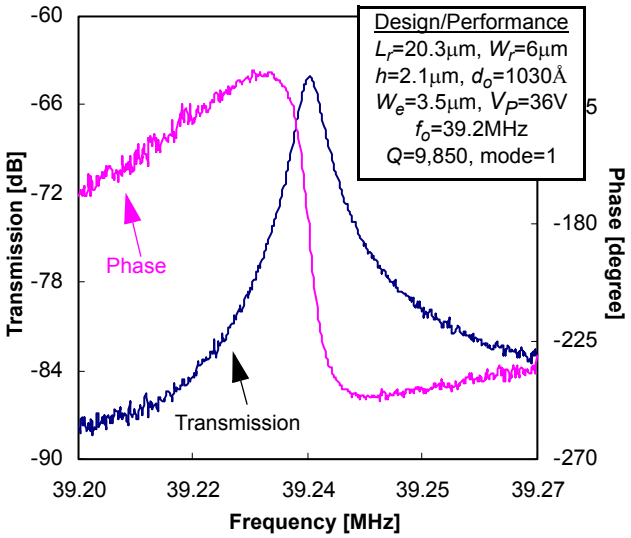


Fig. 13:Fundamental-mode frequency response spectrum of a 101 MHz second-mode free-free beam μresonator.

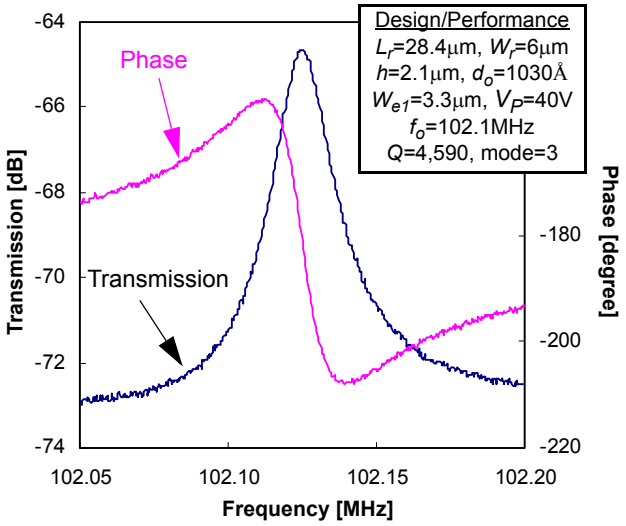


Fig. 14:Frequency spectrum of a 102 MHz third-mode free-free beam μresonator.

Table I compares the measured free-free beam resonator data in Figs. 12 and 14 with theoretical predictions calculated using the equations of Section III, showing very good agreement for motional resistances and for Timoshenko-derived frequencies. The two 100 MHz resonators of the table are most suited for a comparison of second and third-mode performances at the same frequency. Comparing these devices, the third mode $R_x$ is seen to be higher than that for the second mode, even though the extracted gap $d_o$ for the third-mode device is smaller. This reason for this stems from (1) the lower $Q$ of the third-mode, for reasons to be discussed; and (2) the electrode bias and excitation configuration used to measure the third-mode device. In particular, the middle electrode of the third-mode device was not used to excite or sense the device, which reduced the total available drive/sense electrode area below what was possible.

The ~80 MHz devices of Table I allow comparison of fundamental and second-mode resonator performance at the same frequency. Here, the $R_x$ for the second-mode 80 MHz design is seen to be 1.67X lower than that for the fundamental-mode 80 MHz design, which verifies the prediction that the larger electrode area afforded by the second mode device helps to drive down the $R_x$. The higher $Q$ of the second-mode device also contributes to its lower $R_x$.

*A. Q Versus Number of Supports*

The observance of slightly higher $Q$ in the second mode design than the fundamental seems to be tied to the use of fewer support beams in the former, which suggests that vibrational energy losses to the substrate can be minimized by using fewer supports, hence, providing fewer energy-loss paths. To verify the dependence of $Q$ on number of attached supports, Fig. 15 presents a plot of measured $Q$'s for 79.9 MHz second-mode free-free beam resonators with three, four and five supports attached at nodal locations. Here, the $Q$ clearly decreases with an increasing number of supports, suggesting that free-free beam resonators with the highest $Q$ are best achieved with fewer supports.

*B. Dependence of Q on Support Beam Attachment Location*

The high $Q$'s of the free-free beam devices of this work arise largely due precise placement of support beams at nodal locations to eliminate anchor losses. To quantify the importance of

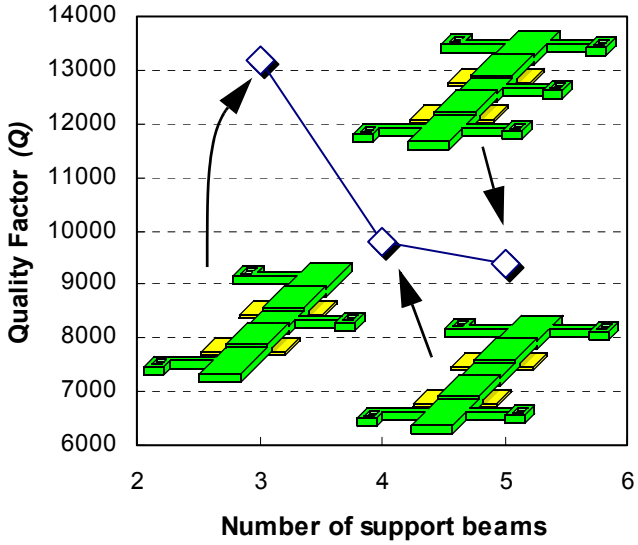


Design Summary
$L_r$=23.7μm, $W_r$=6μm, $h$=2.1μm, $d_o$=1030Å
$L_s$=12.3μm, $W_s$=1.2μm, $W_e$=4.6μm,

Fig. 15:Measured $Q$ vs. number of supports for second-mode free-free beam microresonators with three, four, and five supports attached at the nodal locations.

proper support beam location in setting the ultimate $Q$ of a free-free beam resonator, Fig. 16(a) presents a measured plot of $Q$ versus support beam-to-resonator attachment location $L_A$ (defined in Fig. 16(b)) for several 82 MHz fundamental-mode free-free beam μmechanical resonators with varying $L_A$'s. The SEM of one of the resonators used for this measurement is shown in Fig. 16(c). A strong dependence on the attachment location is seen, where the $Q$ is maximized at 14,000 when the support beam center coincides with the theoretical nodal location, and where attachment at a location just 0.6 μm away from the theoretical node results in a 7X decrease in the $Q$. Fortunately, since all structural geometries are determined in a single masking step for the vertical free-free beam designs of this work, support beam attachments at nodal locations can be very precisely specified via CAD layout, greatly facilitating the ability to achieve high $Q$. Not only is $Q$ maximized when the support beams are attached exactly at the node locations, but the measured resonance frequency of the resonator matches Timoshenko theory only for this case, further stressing the importance of exact support beam attachment.

*C. Dependence of Q on Quarter-Wavelength Support Design*

As discussed in Section III, the beams supporting each of the resonators measured thus far were not only attached to the nodal points of their respective free-free beams, but were also designed with beam lengths corresponding to a quarter wavelength of the operating frequency, with the intent of better isolating the resonator from energy losses through torsional vibrations. To investigate the degree to which quarter wavelength support design is really needed, Fig. 17 presents a measured plot of $Q$ versus support beam length ($L_s$, defined in Fig. 2) for several 60 MHz fundamental-mode free-free beam μmechanical resonators with varying $L_s$'s. As expected, quarter-wavelength design does yield the highest $Q$. However, devices with support beam lengths

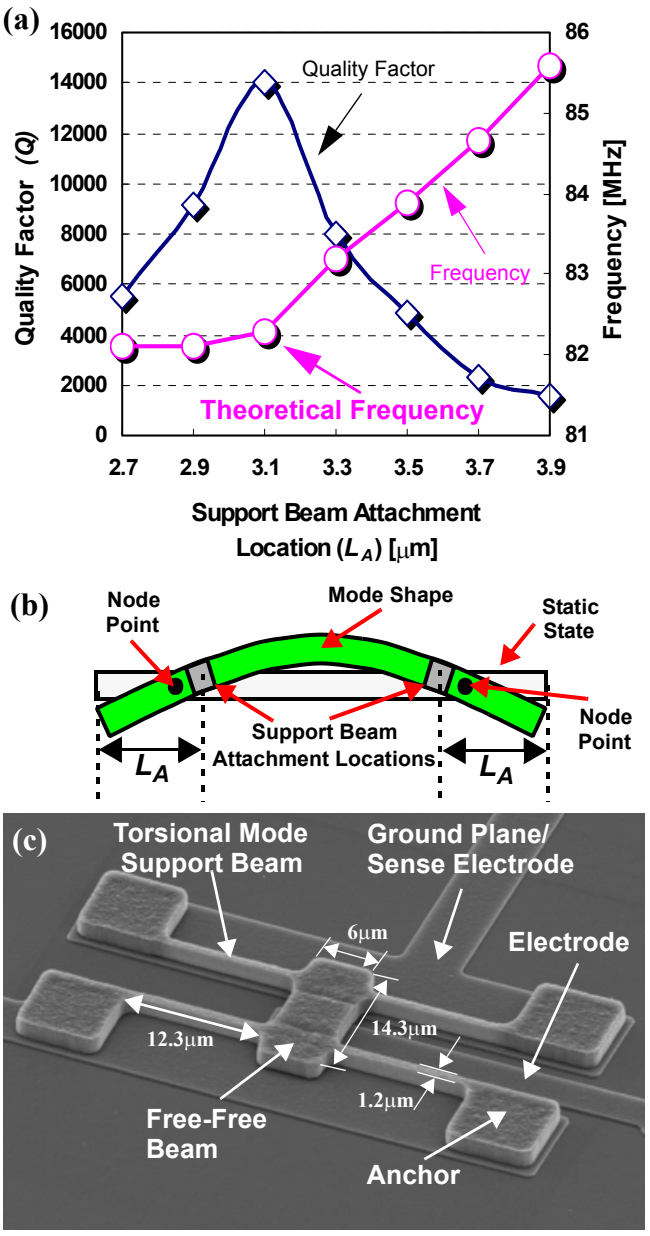


Fig. 16:**(a)** Measured $Q$ versus support beam attachment location ($L_A$) for 82 MHz fundamental-mode free-free beam μresonators with varying $L_A$'s; **(b)** cross-sectional view of a fundamental-mode free-free beam μresonator indicating support beam attachment locations ($L_A$); and **(c)** SEM of one of the 82 MHz fundamental-mode free-free beam μresonators used for this measurement.

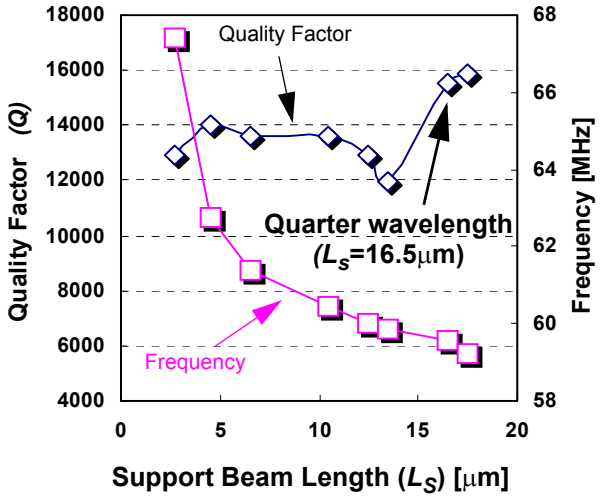


Design Summary
$L_r$=16.5μm, $W_r$=8μm, $h$=2.1μm, $d_o$=1150Å
$W_s$=1.0μm, $W_e$=4.1μm, mode=1

Fig. 17:Measured plots of quality factor and resonance frequency vs. support beam length ($L_s$) for 60 MHz fundamental-mode free-free beam μresonators.

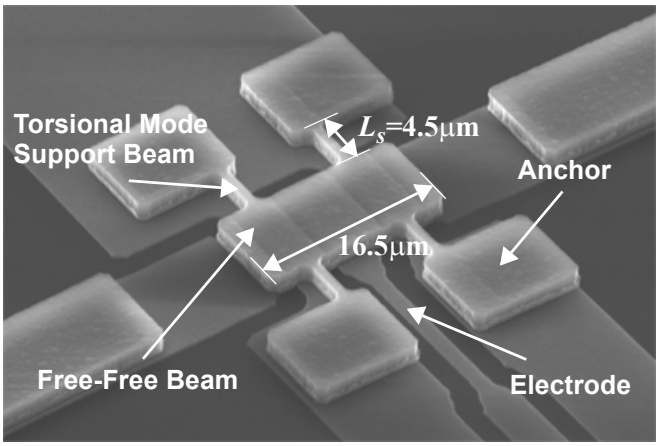


Fig. 18:SEM of a 60 MHz free-free beam with short support beams.

shorter than quarter-wavelength, such as depicted in Fig. 18, still retain more than 87% of the maximum $Q$ value attained with quarter-wavelength supports. Given that devices with shorter support beams can sustain much higher DC-bias voltages without pulling in, and thus, can potentially achieve much smaller series motional resistances $R_x$, the fact that only a small reduction in $Q$ is experienced when quarter-wavelength support dimensions are not used encourages the use of short support beams in future free-free beam resonator designs.

### *D. Temperature Dependence*

Figure 19 presents a plot comparing the frequency vs. temperature measurements for second- and fundamental-mode free-free beam μmechanical resonators. The temperature dependencies for these resonators are similar, with extracted $TC_f$'s (temperature coefficients of frequency) of −13.1 ppm/°C in the second mode and −12.9 ppm/°C in the fundamental mode. It should be noted that the linear dependence of frequency on temperature observed in Fig. 19 should be easier to compensate out than the nonlinear characteristics often seen in macroscopic resonator counterparts, perhaps, giving the free-free beam μmechanical resonators of this work an advantage in applications where temperature-compensation of thermal dependencies is sufficient.

### *E. Operation in Air*

Up to this point, all of the measured curves shown in this paper were done so under 50μTorr vacuum, with the intent of eliminating viscous gas damping mechanism so as to accentuate $Q$-limiting mechanisms associated with support beam design. However, due their high stiffness, the VHF free-free beam resonators of this work operate with internal energies per cycle much

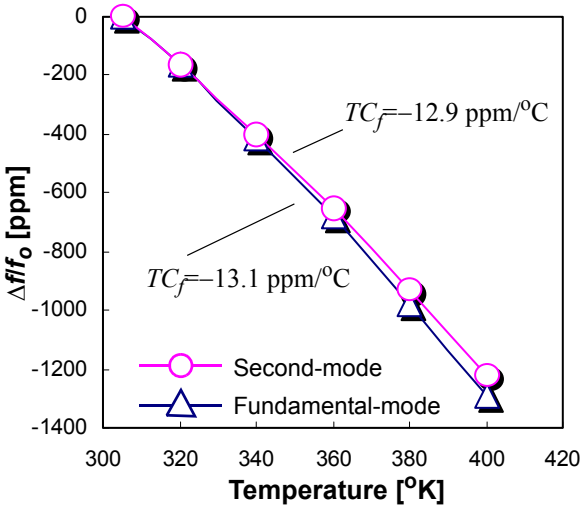


Fig. 19:Measured frequency vs. temperature plots for second- and fundamental-mode free-free beam resonators.

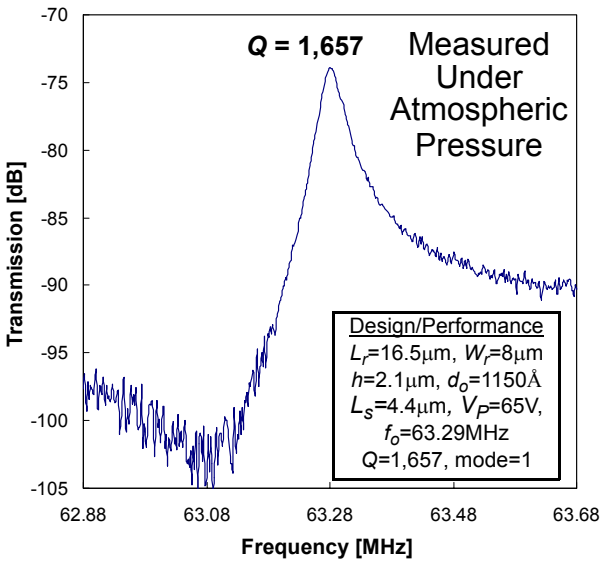


Fig. 20: Frequency characteristic of a 63 MHz fundamental-mode free-free beam μresonator measured under atmospheric pressure.

higher than the energy losses per cycle afforded by viscous gas damping. As such, the resonators of this work actually do not require vacuum to attain reasonably high $Q$'s. To illustrate, Fig. 20 presents the frequency characteristic for a 63 MHz fundamental-mode free-free beam micromechanical resonator measured under atmospheric pressure, yet still showing a $Q$ of 1,657, which is still plenty for use in IF communication applications. This removal of the requirement for vacuum by stiff micron-scale (as opposed to nano-scale) micromechanical resonators has enormous implications, as it allows a substantial reduction in the manufacturing cost of such devices, as well as increases their reliability and lifetime in commercial applications.

## V. Conclusion

Second and third-mode free-free beam microresonators have been demonstrated at frequencies around 100 MHz. Of the two designs, the second-mode is perhaps the optimal for free-free beam μresonators, since its larger device size gives it better linearity and lower $R_x$ than a fundamental-mode design at the same frequency, and its $Q$ is larger and $R_x$ smaller than a third-mode design at the same frequency. Whether second- or third-mode, higher-mode free-free beam μresonators have a usage advantage over fundamental-mode counterparts in that they can provide $0^o$ and $180^o$ input-to-output phase flexibility, and thus, can enable applications (e.g., oscillators, inverting filters) where phase flexibility can be beneficial. In addition, with the availability of short support beam design (which were shown in this paper to be almost as good as quarter-wavelength designs), second-mode free-free beam resonators should now be designable with much lower impedances, making them attractive candidates for use in IF, if not RF, wireless applications.

## Acknowledgment

The authors would like to thank the staff of Solid State Electronics Laboratory (SSEL) at the University of Michigan for fabrication support. This work was supported by DARPA Grant No. F30602-01-1-0573.

## References

[1] C. T.-C. Nguyen, "Transceiver Front-End Architectures Using Vibrating Micromechanical Signal Processors," *Dig. of Papers*, Topical Mtg on Silicon Monolithic IC's in RF Systems, Sept. 12-14, 2001, pp. 23-32.

[2] J. H. Smith, S. Montague, J. J. Sniegowski, J. R. Murray, *et al.*, "Embedded micromechanical devices for the monolithic integration of MEMS with CMOS," *Tech. Digest*, IEEE Int. Electron Devices Meeting (IEDM), Washington, D.C., Dec. 10-13, 1995, pp. 609-612.

[3] A. E. Franke, D. Bilic, D. T. Chang, P. T. Jones, T.-J. King, R. T. Howe, and G. C. Johnson, "Post-CMOS integration of germanium microstructures," *Technical Digest*, 12th Int. IEEE MEMS Conf., Orlando, FA, Jan. 17-21, 1999, pp. 630-637.

[4] A.-C. Wong, Y. Xie, and C. T.-C. Nguyen, "A bonded-microplatform technology for modular merging of RF MEMS and transistor circuits," *Digest of Technical Papers*, the 11th Int. Conf. on Solid-State Sensors & Actuators (Transducers'01), Munich, Germany, June 10-14, 2001, pp. 992-995.

[5] K. Wang, Ark-Chew Wong, and C. T.-C. Nguyen, "VHF Free-Free Beam High-$Q$ Micromechanical Resonators," *IEEE/ASME J. Microelectromech. Syst.*, vol. 8, no. 4, pp. 534-557, Dec. 1999.

[6] J. R. Vig and Y. Kim, "Noise in microelectromechanical system resonators," *IEEE Trans. Utrason. Ferroelec. Freq. Contr.*, vol. 46, no. 6, pp. 1558-1565, Nov. 1999.

[7] S. Timoshenko, *Vibration Problems in Engineering*, 4th ed. New York: Wiley, 1974.

[8] F. D. Bannon III, John R. Clark, and C. T.-C. Nguyen, "High-$Q$ HF Microelectromechanical Filters," *IEEE J. Solid-State Circuits*, vol. 35, no. 4, pp. 512-526, April 2000.

[9] W. Flugge, *Handbook of Engineering Mechanics*. New York: Mc-Graw-Hill, 1962.

[10] H. Nathanson, W. E. Newell, R. A. Wickstrom, and J. R. Davis, Jr., "The resonant gate transistor," *IEEE Trans. Electron Devices*, vol. ED-14, pp. 117-133, Mar. 1967.

[11] H. Guckel, D. W. Burns, H. A. C. Tilmans, D. W. DeRoo, and C. Rutiglano, "The mechanical properties of fine-grained polysilicon: The repeatability issue," in *IEEE Solid-State Sens. Actuator Workshop Tech. Dig.*, Hilton Head, SC, June 1998, pp. 96-99.

[12] R. A. Johnson, *Mechanical Filters in Electronics*. New York: Wiley, 1983.

[13] S. Timoshenko, *Strength of Materials, Part I: Elementary Theory and Problems,* 3rd ed. Melbourne, FL: Krieger, 1958.

[14] W. E. Newell, "Miniaturization of tuning forks," *Science*, vol. 161, pp. 1320-1326, Sept. 1968.